Force generation and wing deformation characteristics of the 'DelFly II' MAV in hovering flight conditions

Perçin, Mustafa; van Oudheusden, Bas; Remes, Bart

Publication date
2015

Document Version
Accepted author manuscript

Published in
International Micro Air Vehicle Conference and Flight Competition

IMAV 2015: International Micro Air Vehicle Conference and Flight Competition,
15-18-Sept. 2015, Aachen, Germany

Force generation and wing deformation characteristics of the 'DelFly II' MAV in hovering flight conditions

M. Percin*, B. W. van Oudheusden and B. Remes
Department of Aerospace Engineering, Delft University of Technology, Kluyverweg 1, 2629 HS Delft, the Netherlands

ABSTRACT

The study investigates the relation between wing deformation and unsteady force generation of the flapping-wing MAV DelFly II in hovering flight configuration. The three-dimensional wing deformation was measured with a stereo-vision system, while fluid forces were acquired simultaneously with a force sensor. Comparison of the results for different flapping frequencies reveals different wing kinematics and deformation characteristics. The high flapping frequency case produces higher forces throughout the complete flapping cycle. Moreover, a phase difference occurs in the variation of the forces, such that the low flapping frequency case precedes the high frequency case. A similar phase lag is observed in the temporal evolution of the wing deformation characteristics, suggesting that there is a direct link between the two phenomena.

1 INTRODUCTION

In flapping-wing flight, structural deformation of the wings is an important aspect in the determination of the aerodynamic performance. The wings deform under the effects of aerodynamic, inertial and elastic forces during the course of a flapping cycle. The complex fluid-structure interaction determines the shape of the flapping wings, which in turn affects the force production. This interrelation is sensitive to the structural properties of the wings (e.g., flexibility and mass distribution) as well as the flapping motion kinematics and wing geometry. In this respect, it is of importance to assess the deformation characteristics of the flapping wings to explain differences in the force production and power consumption of the wings with different structural properties.

The aforementioned fluid-structure interaction is a key element in the aerodynamic performance of flapping-wing MAVs, such as the DelFly that was developed at TU Delft [1]. The DelFly utilizes a bi-plane flapping-wing configuration that performs a clap-and-fling motion as a means of thrust and lift generation. The specific variant the under study here is the DelFly II, henceforth referred to as DelFly for short. The wings of the DelFly are built from flexible Mylar foil reinforced with carbon stiffeners. The use of flexible wing surface results in particular wing flapping characteristics (i.e, clap-and-peel motion), that enhances aerodynamic performance [2, 3].

Initial studies aiming to acquire wing deformations in flapping-wing flight were conducted on insects. The deformation characteristics of MAV wings bear resemblance to that of the insects wings in view of their light construction ($0.5 - 5$ % of the total body mass for insects [4] and 7 % of the total mass for the DelFly II). Moreover, the wing deformations are predominantly passive in both cases as there is no muscular control of the wing flexure in insect flight [5]. Early studies provided essentially qualitative observations and reported the occurrence of considerable camber and spanwise twist in several insects, e.g., locusts [6, 7, 8], hawkmoths [9], butterflies [10], crane flies, hoverflies and bees [2] as cited in [11]. However, the role of twist and camber in the force production of insect flight were not fully understood due to complexity of the structural deformations and qualitative nature of the observation methods. Wang et al. [12] applied a projected comb-fringe technique to acquire wing kinematics, deformations, body position and attitude of a free-flying dragonfly. Their measurements revealed that both forewing and hindwing have positive camber during the downstroke, whereas negative camber is present during the upstroke for a short duration. In order to investigate the effect of camber on force generation, they conducted a two-dimensional numerical simulation of a single airfoil undergoing measured kinematics of the dragonfly's forewing in the forward flight configuration. These simulations revealed that the flexible airfoil with the time-varying camber generates higher forces both in lift and drag than the rigid wing in contrast to some previous studies which reported that camber deformation has a minor effect on aerodynamic forces at high angles of attack [13, 14]. A similar numerical study by Du and Sun [15] showed that twist has a marginal influence on the force generation, whereas camber deformation has a significant effect. A flapping wing with 6 % camber and $20°$ twist produces 10 % to 20 % more force and has approximately 10 % higher lift to drag ratio compared to a rigid flat-plate wing. Moreover, the power required to drive the wings is reduced by 16 %.

The relationship between the structural deformation of the flapping flexible wings and aerodynamic forces has been investigated also by use of mechanical flapping-wing systems and flapping-wing MAVs. Wu et al. [16] tested four flexible membrane wings with different stiffness characteristics by measuring structural deformations and unsteady forces in

*Email address: m.percin@tudelft.nl

hovering configuration. The three-dimensional coordinates of a random speckle pattern on the wing was measured by stereo triangulation using four cameras. They reported that wings with stronger skeletal reinforcement produce higher thrust (corresponding to lift or X-force in hovering configuration) at relatively high frequencies (e.g., above 25 Hz) and the inverse at lower flapping frequencies. They noted that thrust increases quadratically with flapping frequency, however this increase is degraded to a linear trend in the case extreme twisting deformations occur. They also stated that the chordwise stiffness should be orders of magnitude lower than the spanwise stiffness in order to achieve greater performance in terms of efficiency and thrust effectiveness. Passive wing deformations of the DelFly II flapping wings have been subject to a number of experimental studies [17, 18]. The wing shape was obtained from the images of particle image velocimetry (PIV) measurements conducted at a certain spanwise location so that no information on spanwise variation was available for further analysis. Nevertheless, these planar observations revealed the occurrence of the clap-and-peel mechanism, leading and trailing edge paths, presence of a significant wing camber [17] and difference between the deformation-wise behaviours of the original and improved DelFly wings [18].

It is evident that structural properties of the wings are highly influential parameters in flapping-wing aerodynamics. Assessment of their impact on the generation of forces is essential for further optimization of the flapping-wing MAV designs. Notwithstanding the number of studies aiming to assess wing deformations on biological flyers, the relation between the wing shape and unsteady forces in flapping-wing MAVs, particularly in biplane configuration where wing-wing interaction further complicates the fluid-structure interaction, is not fully resolved. In this respect, the specific aim of this study is to explore the relation between the aerodynamic performance and wing structural deformation characteristics of the flapping-wing MAV DelFly II in hovering flight configuration by means of simultaneous force and wing deformation measurements.

2 Experimental Setup

2.1 Experimental model and force measurement system

In the measurements, a full-scale DelFly without a tail was used as an experimental model in hovering flight configuration. It has a bi-plane flapping-wing configuration with wings which consists of 10-μm thick Mylar foil to form the wing surface, a D-shaped carbon rod to form the leading edge and circular carbon rods placed on the wing surface to provide extra stiffness. The semi-wing span (R) is 140 mm and the model has an overall mass of approximately 11 grams. A custom-made brushless motor with a motor controller, a gear system and a crank shaft mechanism are used to drive the wings in flapping motion. More detailed information on the DelFly can be found in [1].

Six components of forces and moments were measured at a recording rate of 12.5 kHz by use of an ATI Nano17 Titanium force sensor. The sensor is calibrated to have a maximum sensing value of 32 N in x,y and 56.4 N in z direction with a measurement uncertainty of 1 % of the full-scale load with 95 % confidence level. In the hovering flight configuration the DelFly is oriented vertically (x_b axis is parallel to y axis, see Fig. 1a), therefore the X-force that is oriented in the x_b direction of the body coordinate system is the main focus of interest because it is the force component that balances the weight of the DelFly.

The raw force data was filtered to remove noise and vibration components in the signal, by means of a Chebyshev Type II low-pass filter with -80 dB attenuation of the stop band. A forward-backward filtering technique was used in order to prevent time shift of the data. The cut-off frequency was selected based on the flapping frequency to allow the first two harmonics of the force oscillations to be present in the resultant data as these modes were found to be related to aerodynamic forces, as verified by flapping tests carried out under vacuum conditions [19].

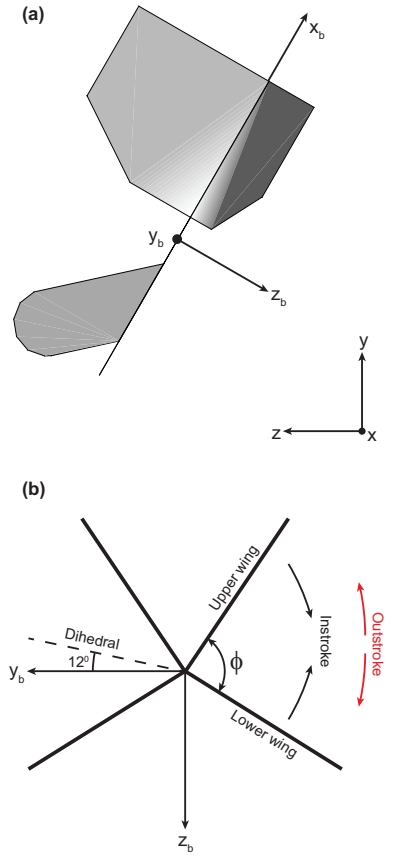

Fig. 1: **a** Sketch of the DelFly II in flight with inertial (x, y, z) and DelFly body (x_b, y_b, z_b) coordinate systems, **b** front view of the wing leading edges

2.2 Experimental setup for wing deformation measurements

The simultaneous force and wing deformation measurements were performed in a quiescent environment (simulating the hovering flight configuration) on the experimental DelFly model mounted on a balance mechanism that is equipped with the force sensor (Fig. 2a).

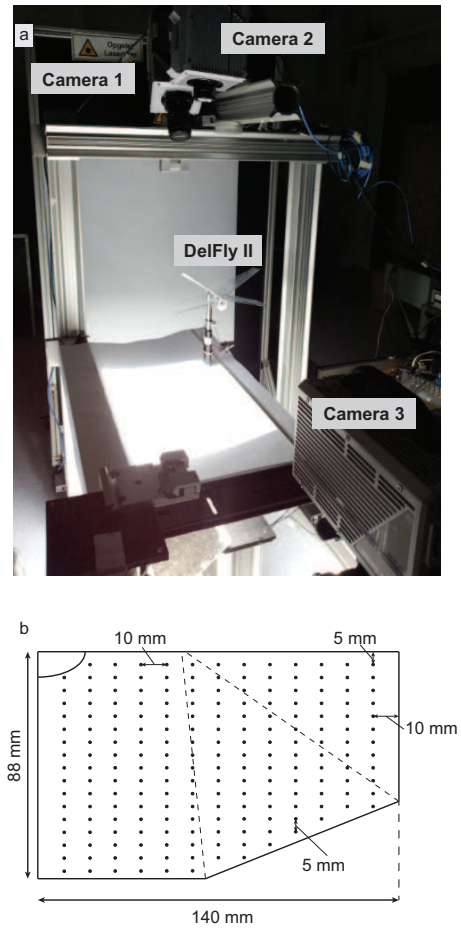

Fig. 2: **a** Experimental setup for the wing structural deformation measurements, **b** sketch of the wing layout with circular markers

Structural deformations of the upper wing were measured for different wing types in a flapping frequency range of $7 - 13$ Hz. However the discussion in this paper is restricted to data of a single wing type and the comparison of two frequencies (viz., 7.5 and 12 Hz) to better appreciate the differences between the structural deformations. For each case, the three-dimensional wing geometry was reconstructed for twenty phases in the flapping cycle. The marker positions one time step (i.e., 1/image recording frequency) before and after a given phase were also reconstructed to assess the velocity of the markers at that instant.

A structured grid of circular dots with an approximate diameter of 1 mm were marked on the Mylar surface of the right upper wing during the manufacture process. The distance between the markers is 5 mm in the chordwise direction and 10 mm in the spanwise direction (see Fig. 2b). The first horizontal line of markers is positioned at 5 mm distance from the leading edge, whereas the distance between the outermost vertical line and the wing tip is 10 mm. This gives a total number of 200 markers on the present wing configuration. Nevertheless, the innermost line of markers had to be omitted from the detection process due to their proximity to the DelFly body, which results in the loss of these markers from the vision of the cameras at numerous phases of the flapping motion.

The images of the markers were captured with two CMOS cameras with a maximum resolution of 1024×1024 pixels and a pixel pitch of 20 μm. The cameras were arranged at an angle of 30° with respect to each other (Fig. 3a). Each camera was equipped with a Nikon lens (with an objective focal length of 60 mm for the Camera 1 and 50 mm for the Camera 2) with a numerical aperture of $f\# = 16$. A Scheimpflug adapter was used on the Camera 1 to align the mid-plane of the measurement volume with the focal plane. The digital resolution is approximately 7.5 pixels/mm. A measurement volume of $150 \times 150 \times 140$ mm in size was positioned with its lowermost plane at the same height with the DelFly body so as to cover the complete stroke of the upper wing (see Fig. 3a and b). In order to provide a clear image of the markers and improve the detectability, a back-lighting illumination technique was used. For this purpose, a sheet of white paper was laid underneath the DelFly model, onto which the light beam produced by an HMI spotlight (JB System FSP 757 MSR Followspot) was reflected to generate a white diffused background in a dark environment. Simultaneously, a third camera, which was placed normal to the flapping wings in front view (see Figs. 2 and 3a), captured the motion of the leading edges of the left upper and lower wings in order to determine the stroke angle. The images of the markers and the leading edges were acquired in an image recording frequency range of 1-2 kHz.

Image acquisition, volume calibration and image preprocessing were performed in the PIV software LaVision DaVis $8.1.6$. The measurement volume was calibrated by scanning a three-dimensional plate through the volume in depth of 140 mm with steps of 20 mm. The mapping information between the image coordinates and the physical coordinates for each camera was exported from DaVis $8.1.6$ with a resolution of 1.3 mm in each direction. The black and white images were inverted in color and preprocessed with background intensity removal and a Gaussian smooth with 9×9 kernel size.

An in-house developed Matlab code was used for the detection of the markers and the reconstruction of their three-dimensional coordinates. The circular Hough transform technique was utilized for the initial detection of the wing markers in both images. Then, the positioning of the image coordi-

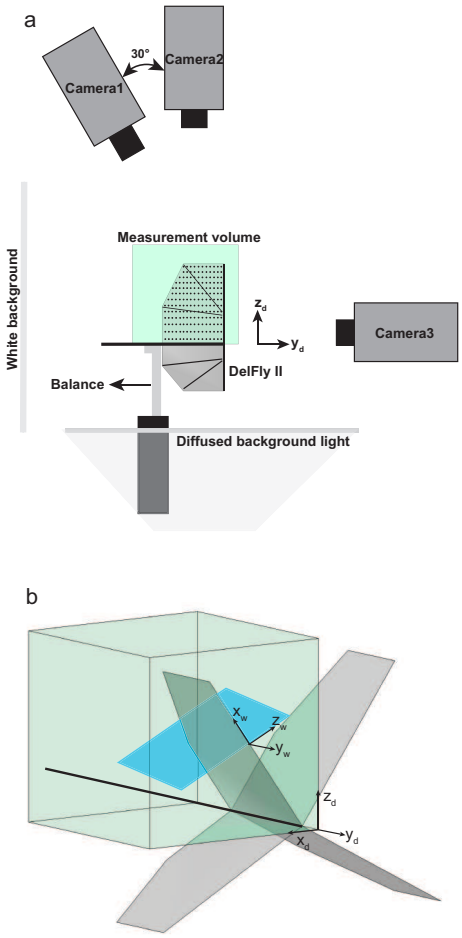

Fig. 3: **a** Sketch of the side view of the experimental setup; **b** schematic representation of the measurement volume (*in green*), the global coordinate system for the reconstruction of the three-dimensional marker coordinates (x_d, y_d, z_d), the wing coordinate system for the calculation of wing profile shape at a given spanwise location (x_w, y_w, z_w), the $y_w - z_w$ plane in which the wing deformations are depicted (*in blue*)

nates of the marker centers were further improved by calculating the centroid of the intensity distribution for each detected marker. Subsequently, the matching process between the detected markers in the two images was performed based on the known structural grid properties and three reference points defined in the both camera images at the beginning of the process. The image coordinates of the markers were then triangulated by use of the mapping information of the cameras to acquire the three-dimensional coordinates. A midpoint triangulation technique was used and the closest distance between projection lines for each marker was defined as a measure of uncertainty. The reconstructed markers with more than 1.4 mm distance between the projection lines are detected as outliers and excluded from the further analysis. The average uncertainty in the detection and triangulation of the resultant marker coordinates is about 0.1 mm for the cases considered in this study. The three-dimensional coordinates of the markers acquired in the global camera coordinate system (x_d, y_d, z_d) are transformed into the wing coordinate system $(x_w, y_w, z_w$ with x_w oriented parallel to the leading edge), see Fig. 3b, in order to calculate the wing profile properties, i.e., camber, angle of attack, trailing edge deformation and the width of the suction column at a given spanwise location. The deformed wing profiles at different phases of the wingbeat cycle are depicted in $z_w - y_w$ plane (blue plane in Fig. 3b). Although Fig. 3 indicates the origin of the wing coordinate system to lie on the wing leading edge, in the following wing representations the reference position $z_w = 0$ is relocated to the dihedral plane.

The first and last markers on the chord line are used to represent the leading and trailing edges and to calculate their kinematics, respectively. At a given instant of the flapping motion, the chord line is defined as the line connecting the leading edge and trailing edge markers at a specified spanwise position (Fig. 4). The camber of the wing profile is defined as the maximum distance between the chord line and the markers along the profile. The geometric angle of attack (α) is the angle between the chord line and the stroke velocity vector of the leading edge marker $(\vec{U}_{LE})$. The maximum horizontal suction column width is indicative of the area with its normal oriented in the X-force direction and defined as the maximum horizontal distance between the leading edge marker and the other detected markers. All parameters with the dimension of length are normalized by the mean chord length of the wing and denoted with superscript "*".

3 Results

Wing profiles throughout a flapping cycle at three different spanwise locations (i.e., $0.5R$, $0.71R$ and $0.93R$) of the wing for flapping frequencies of 7.5 and 12 Hz are shown in Fig. 5. Note that the color of the wing profile changes from black to light gray as the wing proceeds in motion starting from the beginning of the instroke.

It is clear that in addition to the sweeping (driven by the flapping system) and pitching (occurs passively due to combination of aerodynamic, inertial and elastic forces) motion, the wings also undergo a heaving motion, which is better visible closer to the wing tip (see the spanwise position of $0.93R$ in Fig. 5). The heaving motion kinematics in combination with the sweeping motion determines the trajectory of the leading edge, which plays an important role in the generation of forces by changing the effective angle of attack of the wing during the sweeping motion. For instance at this spanwise position, the downward motion of the wing in the $-y_w^*$ direction increases the angle of attack which can promote the formation of LEV circulation and thus force generation [20, 21, 22]. The amplitude of the heaving motion is approximately $0.07\overline{c}$ and $0.085\overline{c}$ for the flapping frequencies of 7.5 and 12 Hz, re-

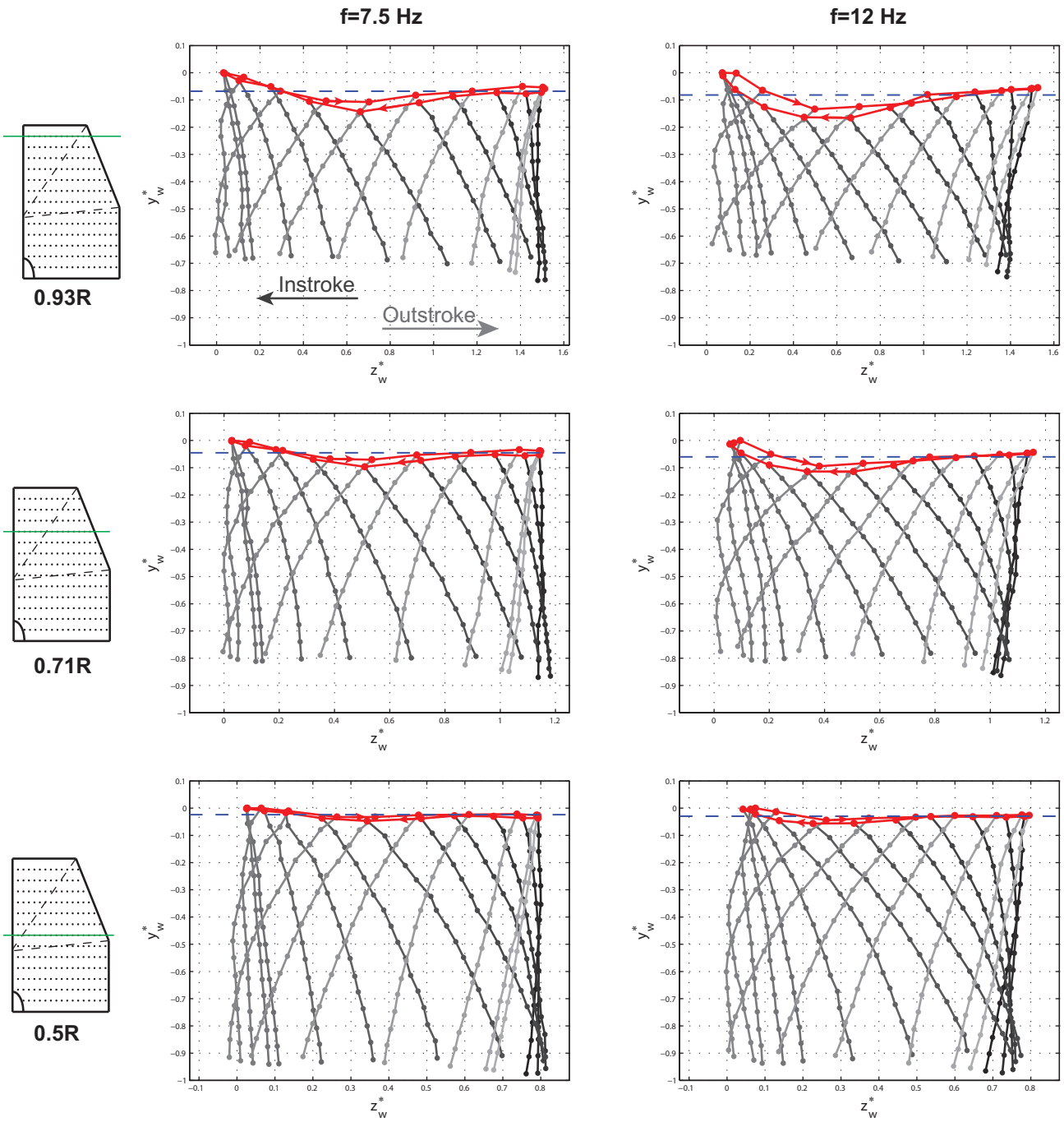

Fig. 5: Wing profiles throughout the flapping cycle for the flapping frequencies of 7.5 Hz (*left*) and 12 Hz (*right*) at three different spanwise locations: $0.93R$ (*first row*); $0.71R$ (*second row*); $0.5R$ (*third row*). Note that the color of the wing profile changes from black to light gray as the wing proceeds in motion starting from the beginning of the instroke. The leading edge and its trajectory is depicted in red, whereas the mean stroke plane is represented with blue dashed line.

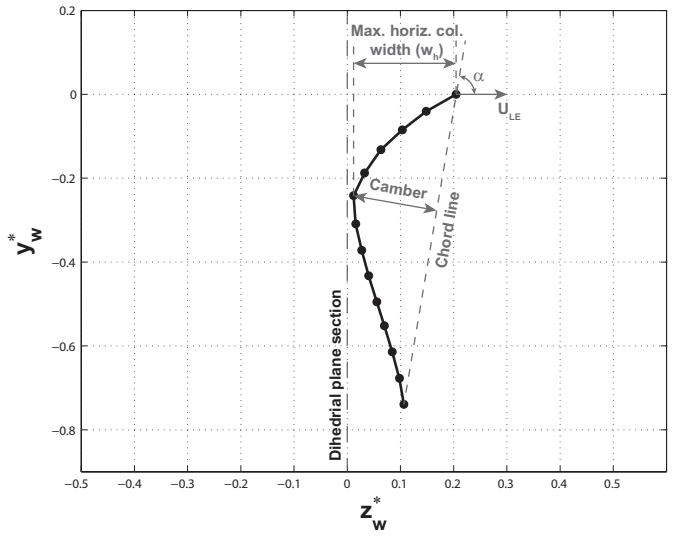

Fig. 4: Wing profile definitions depicted on the wing profile at 70 % spanwise position of the Ref10 wing flapping at 12 Hz at the phase of $t^* = 0.65$ plotted in the non-dimensional wing coordinate system x^*_w, y^*_w, z^*_w (normalized by the mean chord length, $\overline{c} = 80$ mm)

spectively. For the low flapping frequency case, the leading edge marker heaves downwards (for $0.08\overline{c}$) until $t^* = 0.25$ and then start moving upwards (for $0.14\overline{c}$), which lasts until the stroke reversal. In combination with the decreasing sweeping velocity of the wing, this upward heaving motion during the second half of the instroke further decreases the effective angle of attack. During the outstroke, the wing first heaves down for $0.1\overline{c}$ during the first $t^* = 0.15-0.2$ and subsequently moves upwards for $0.05\overline{c}$ in the remaining part of the outstroke. The high flapping frequency case mostly differs in terms of heaving amplitudes and kinematics in the second half of the instroke. Similar to the low frequency case, the wing plunges downwards until $t^* = 0.25$ during the instroke but then follows an exponential curve upwards rather than a linear path. Such a pattern is more favorable because most of the vertical motion occurs toward the end of the stroke when the sweeping velocity is rather low so that the force generation is small as well. In this way, the negative effect of the upward heaving motion is excluded from the energetic part of the instroke. This is the underlying strategy behind the figure-of-eight pattern in which the wing heaves only downwards during both strokes and performs the upward heaving movements only during the stroke reversals. It should also be noted that the leading edge trajectory is rather flat about the stroke reversal from outstroke to instroke. Evidently, the heaving motion works in favour of increasing effective angle of attack during the first half of both instroke and outstroke phases for this case together with the increasing stroke (sweeping) velocity at the outer sections of the wing. However, the amplitude of the heaving motion decreases down to $0.02\overline{c}$ and $0.03\overline{c}$ already at $0.5R$ position for the flapping frequencies of 7.5 and 12 Hz, respectively.

Another prominent feature that comes out from the comparison of the two cases is the difference between the deformation characteristics of the wing around the two stroke reversals. At the beginning of the instroke, it is clear that the profile is mostly non-deformed and displays some waviness particularly at the out-most spanwise position. In this period, the trailing edge moves more outwards in the low flapping frequency case. This can be attributed to relatively small chordwise deformation of the wing compared to the high flapping frequency case and as a result changing balance between the aerodynamic, inertial and elastic forces. On the other hand, at the start of the outstroke, the wing displays a significantly different deformation behaviour due to the wing-wing interaction (clap-and-peel motion) occurring during this phase: the wing starts moving outwards at the leading edge side, whereas the lower-chord side of the wing is being attracted toward the mirror wing due to formation of a low-pressure region between the wings. This interaction results in a peel-like deformation that increases the effective horizontal column width as well as forming a cambered wing profile.

It is of importance to assess the influence of aforementioned differences on the resultant forces to gain a better understanding of the DelFly force generation mechanisms. In Fig. 6, the X-force variation during a flapping period is plotted for the two cases. Clearly, the higher flapping frequency case produces a higher X-force during the complete flap cycle. The comparison also reveals that there is a phase difference in the production of the forces such that the low flapping frequency case precedes high frequency case by a non-dimensional time difference of $t^* = 0.05$.

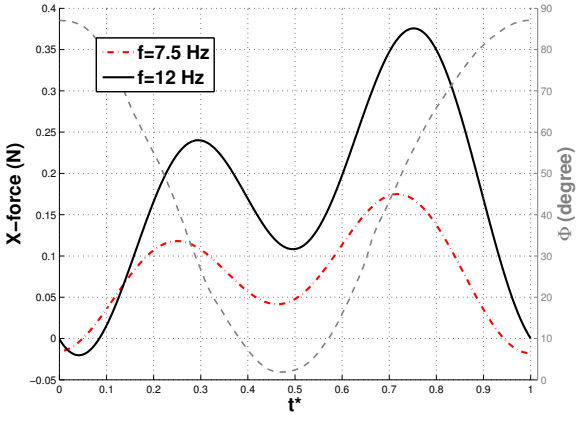

Fig. 6: Temporal variation of the X-force component complemented with the variations of the upper wing angle (*dashed gray*) during a wing-beat cycle for the flapping frequencies of 7.5 and 12 Hz

In order to connect the wing deformation to the observed X-force history, the angle of attack variations of the two cases at the spanwise location of $0.71R$ are plotted in Fig. 7. The angle of attack values greater than $90°$ occurs during the stroke reversals and indicate the wings performing delayed rotation, which can be detrimental for the force generation [23, 24]. The average uncertainties in the reported angle of attack values is $\delta\alpha = 0.3°$ with 95 % confidence level. The comparison of the angle of attack variations reveals that the wing orients such that it attains a positive angle of attack in the upcoming stroke faster for each of the stroke reversals in the low flapping frequency case. In other words, the wing performs a delayed rotation during stroke reversals in both cases but with a larger phase delay in the high flapping frequency case. As the wing accelerates in sweeping motion both during the instroke and the outstroke, the wing deforms more in the high frequency case due to relatively high fluid forces, resulting in lower angle of attack values than for the low frequency case.

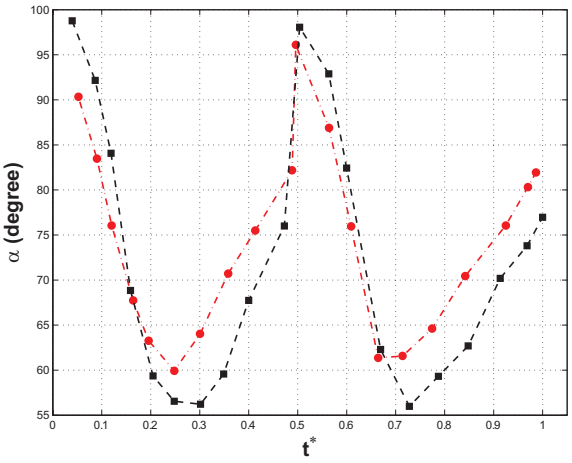

Fig. 7: Temporal variation of the angle of attack (α) during a flapping cycle for the flapping frequencies of 7.5 and 12 Hz

The higher deformation at high flapping frequency also brings in larger suction width (w^*) throughout most of the wing-beat cycle (Fig. 8). The phases of the occurrences of the maximum suction areas during the flapping cycle show a good correlation with those of X-force in both cases. There is 4 and 7 % of $\bar{c}$ difference between the maximum suction column widths of the two cases during the instroke and outstroke, respectively. The phase difference between the X-force variations of the two cases is also present in the angle of attack and suction column width variations. Apparently, the delay in the reorientation of the wing surface during the stroke reversals retards the progress of the wing profile parameters and hence the X-force generation.

Another important wing profile property that influences

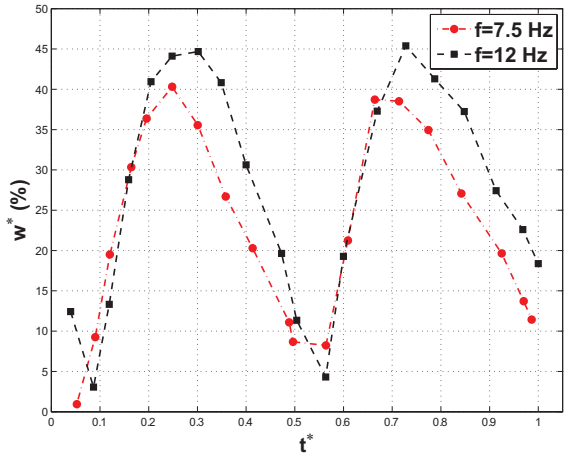

Fig. 8: Temporal variation of the horizontal suction column width (w^*) during a flapping cycle for the flapping frequencies of 7.5 and 12 Hz

the force generation is the wing camber, variation of which at the $0.71R$ spanwise location during a flapping cycle for the two flapping frequency cases is shown in Fig. 9. For a given flapping frequency, the wing camber peaks twice during a period of a flapping motion both happening at the early stages of the instroke ($t^* = 0.1 - 0.2$) and the outstroke ($t^* = 0.6$). Due to the wing-wing interaction and associated pressure fields, the camber during the outstroke reaches significantly higher values than those during the instroke. The wing profile has a maximum camber value (defined relative to the local chord length c) of 11 % at the $0.54c$ chord location ($c = 0.75\bar{c}$) during the instroke, whereas it is 21 % with the camber location of $0.35c$ ($c = 0.79\bar{c}$) during the outstroke. Apparently, the clap-and-fling motion with flexible wings (i.e., clap-and-peel motion) results in the formation of a wing profile with a significant camber, which is reported to be favorable in terms of force generation [15, 25].

4 Conclusions

Unsteady forces and three-dimensional wing deformations of the flapping-wing MAV 'DelFly II' were acquired in hovering flight configuration for flapping frequencies of 7.5 and 12 Hz. A stereo-vision system of two high-speed cameras, was utilized to record images of 200 circular dots marked on the upper wing surface. In order to reconstruct the three-dimensional wing geometry. Simultaneously, forces and moments were acquired with a force sensor. Both measurements were synchronized to assess the relation between the wing deformation and force production.

Comparison of the wing profiles throughout a flapping cycle of the two cases reveals differences in wing kinematics and deformation characteristics. The wing undergoes a larger amplitude heaving motion in the higher flapping frequency

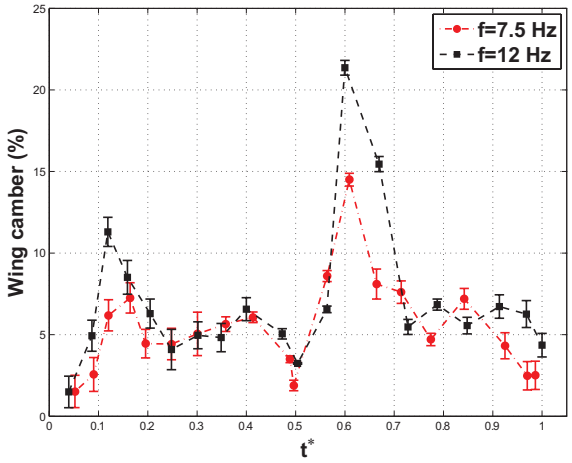

Fig. 9: Temporal variation of the wing camber (defined relative to the local chord length c) during a flapping cycle for the flapping frequencies of 7.5 and 12 Hz

case. In addition to the amplitude, the leading edge trajectory pattern differs between the cases. The heaving motion is quite linear particularly in the second half of the instroke and in the first half of the outstroke for the low frequency case, whereas the leading edge follows a rather curved path in the high frequency case.

The high flapping frequency case produces higher X-force throughout the complete flapping cycle as expected (relative difference of approximately 76 % in the flap-averaged forces). Moreover, there is a phase difference in the variation of the forces such that the low flapping frequency case precedes the high frequency case by a non-dimensional time shift of $t^* = 0.05$. A similar phase lag was also observed in the temporal evolutions of the angle of attack and horizontal suction column width. It is shown that the wing performs a delayed rotation in both cases yet with a larger delay in the high flapping frequency case. This results in a delay also in the progress of the wing profile parameters and hence the X-force generation. In general, the wing deforms more while flapping at 12 Hz due to relatively higher fluid forces. This results in lower angle of attack and higher suction column width values for the high flapping frequency case. Temporal variations of the wing camber, on the other hand, shows that the wing has significantly larger camber during the outstroke in both cases, which is attributed to the effects of wing-wing interaction occurring during the stroke reversal from instroke to outstroke (i.e., clap-and-peel motion).

REFERENCES

[1] G.C.H.E. de Croon, M.A. Groen, C. De Wagter, B.D.W. Remes, R. Ruijsink, and B.W. van Oudheusden. Design, aerodynamics, and autonomy of the DelFly. *Bioinspiration and Biomimetics*, 7(2), 2012.

[2] C. P. Ellington. The Aerodynamics of Hovering Insect Flight. III. Kinematics. *Philosophical Transactions of the Royal Society B: Biological Sciences*, 305(1122):41–78, February 1984.

[3] Laura A Miller and Charles S Peskin. Flexible clap and fling in tiny insect flight. *The Journal of experimental biology*, 212(19):3076–90, October 2009.

[4] C. P. Ellington. The Aerodynamics of Hovering Insect Flight. II. Morphological Parameters. *Philosophical Transactions of the Royal Society of London. Series B, Biological Sciences (1934-1990)*, 305:17–40, 1984.

[5] S. A. Combes and T. L. Daniel. Flexural stiffness in insect wings II. Spatial distribution and dynamic wing bending. *Journal of Experimental Biology*, 206(17):2989–2997, September 2003.

[6] Martin Jensen. Biology and physics of locust flight. iii. the aerodynamics of locust flight. *Philosophical Transactions of the Royal Society B: Biological Sciences*, 239(667):511–552, 1956.

[7] P. S. Baker and R. J. Cooter. The natural flight of the migratory locust, Locusta migratoria L. - I. Wing movements. *Journal of Comparative Physiology*, 131(1):79–87, 1979.

[8] Michael Wortmann and Wolfram Zarnack. Wing Movements and Lift Regulation in the Flight of Desert Locusts. *The Journal of Experimental Biology*, 182:57–69, 1993.

[9] Alexander P Willmott and Charles P Ellington. The mechanics of flight in the hawkmoth manduca sexta. i. kinematics of hovering and forward flight. *The Journal of Experimental Biology*, 200(21):2705–2722, 1997.

[10] Robin J Wootton. Leading edge section and asymmetric twisting in the wings of flying butterflies (insecta, papilionoidea). *The Journal of Experimental Biology*, 180(1):105–117, 1993.

[11] Simon M Walker, Adrian L R Thomas, and Graham K Taylor. Photogrammetric reconstruction of high-resolution surface topographies and deformable wing kinematics of tethered locusts and free-flying hoverflies. *Journal of the Royal Society, Interface / the Royal Society*, 6(August 2008):351–366, 2009.

[12] Hao Wang, Lijiang Zeng, and Chunyong Yin. Measuring the body position, attitude and wing deformation of a free-flight dragonfly by combining a comb fringe pattern with sign points on the wing. *Measurement Science and Technology*, 13(6):903, 2002.

[13] M. H. Dickinson and Karl G. Götz. Unsteady aerodynamic performance of model wings at low Reynolds numbers. *Journal of Experimental Biology*, 174:45–64, 1993.

[14] Shigeru Sunada, Keiji Kawachi, Isao Watanabe, and Akira Azuma. Fundamental analysis of three-dimensional near fling. *The Journal of Experimental Biology*, 183:217–248, 1993.

[15] Gang Du and Mao Sun. Effects of unsteady deformation of flapping wing on its aerodynamic forces. *Applied Mathematics and Mechanics (English Edition)*, 29(20070404):731–743, 2008.

[16] Pin Wu, Peter Ifju, and Bret Stanford. Flapping Wing Structural Deformation and Thrust Correlation Study with Flexible Membrane Wings. *AIAA Journal*, 48(9):2111–2122, September 2010.

[17] K.M.E. De Clercq, R. de Kat, B. Remes, B.W. van Oudheusden, and H. Bijl. Aerodynamic experiments on DelFly II: Unsteady lift enhancement. *International Journal of Micro Air Vehicles*, 1(4):255–262, 2009.

[18] Mark Groen, Bart Bruggeman, Bart Remes, Rick Ruijsink, BW Van Oudheusden, and Hester Bijl. Improving flight performance of the flapping wing MAV DelFly II. In *Int. Micro Air Vehicle Conf. and Competition (IMAV 2010)(Braunschweig, Germany)*, 2010.

[19] M. Groen. PIV and force measurements on the flapping-wing MAV DelFly II. Master's thesis, Delft University of Technology, 2010.

[20] O. Baskan. Experimental and numerical investigation of flow field around flapping airfoils making figure-of-eight in hover. Master's thesis, Middle East Technical University, 2009.

[21] S. P. Sane and M. H. Dickinson. The control of flight force by a flapping wing: lift and drag production. *The Journal of Experimental Biology*, 204(Pt 15):2607–26, August 2001.

[22] Fritz-Olaf Lehmann and Simon Pick. The aerodynamic benefit of wing-wing interaction depends on stroke trajectory in flapping insect wings. *The Journal of Experimental Biology*, 210(Pt 8):1362–77, April 2007.

[23] M. H. Dickinson, Fritz-Olaf Lehmann, and S. P. Sane. Wing Rotation and the Aerodynamic Basis of Insect Flight. *Science*, 284(5422):1954–1960, June 1999.

[24] S. P. Sane and M. H. Dickinson. The aerodynamic effects of wing rotation and a revised quasi-steady model of flapping flight. *The Journal of Experimental Biology*, 205(Pt 8):1087–96, April 2002.

[25] John Young, Simon M Walker, Richard J Bomphrey, Graham K Taylor, and Adrian L R Thomas. Details of insect wing design and deformation enhance aerodynamic function and flight efficiency. *Science*, 325(September):1549–1552, 2009.